Energy LAB

RESEARCH ARTICLE

Energy Lab 2023, 1, 220022

Intermetallic PtTe metallene for formic acid oxidation assisted electrocatalytic nitrate reduction

Qingling Hong[1], Boqiang Miao[1], Tianjiao Wang[1], Fumin Li[2*] and Yu Chen[1*]

Development of highly efficient electrocatalysts for selective electroreduction of nitrate is of great significance. In this work, the ultrathin intermetallic platinum-tellurium metallene (PtTe-ML) with atomic thickness is synthesized by simple liquid-phase chemical reduction. The introduction of Te atoms can sharply weaken the catalytic activity of Pt for the hydrogen evolution reaction. And, PtTe-ML exhibits superior catalytic activity for the nitrate reduction reaction (NO_3^--ERR) than Pt black. In 0.5 M H_2SO_4 solution, PtTe-ML achieves an effective ammonia (NH_3) production rate of 2.32 mg h^{-1} mg_{cat}^{-1} and a Faradic efficiency of 95.5% at –0.04 V potential for NO_3^--ERR. Meanwhile, the entry of Te atom isolates the continuous Pt active site and increases the proportion of the direct dehydrogenation pathway of the formic acid oxidation reaction (FAOR). Therefore, PtTe-ML also exhibits excellent FAOR activity due to the optimization of FAOR pathway. Then, anodic FAOR with low anodic oxidation potential is used to replace the oxygen evolution reaction with slow kinetic, so that the total electrolytic voltage of conventional electrochemical NH_3 production can be effectively reduced. Consequently, the bifunctional PtTe-ML electrocatalyst requires only 0.4 V total voltage for FAOR assisted NH_3 electroproduction. This work demonstrates a reaction coupling strategy to significantly improve the utilization rate of electric energy in electrochemical synthesis.

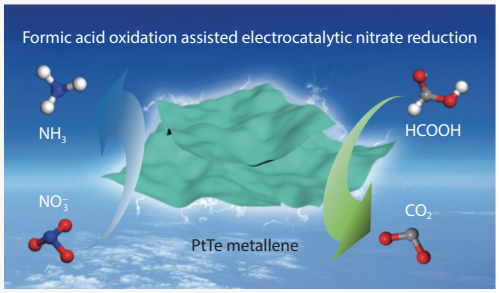

Nitrate (NO_3^-) is one of the main species of nitrogen pollutants. The increasing level of NO_3^- pollution in water seriously endangers the environment and human health.[1,2] NO_3^- is difficult to recover, while ammonium nitrogen (NH_4^+) can be recovered directly as fertilizer or converted to ammonia (NH_3). NH_3 is expected to be the next generation of energy carriers because of its high energy density and no pollution emissions.[3–5] Currently, industrial NH_3 production is mainly by the Haber-Bosch method through the combination reaction of nitrogen (N_2) and hydrogen (H_2) under high temperature and pressure conditions. However, this method has harsh synthesis conditions and high energy consumption. As an alternative, the electroreduction of N_2 to NH_3 has also received attention in recent years. However, the yield and Faradaic efficiency of NH_3 remain limited in most studies due to the high N≡N dissociation energy (941 kJ mol^{-1}) in N_2 molecule, the interference of hydrogen evolution reaction (HER) and the solubility limitation of N_2 in H_2O. In contrast, the N=O bond in NO^- has a lower dissociation energy (204 kJ mol^{-1}) than that of the N≡N bond.[6–8] Thus, the electrochemical NO_3^- reduction reaction (NO_3^--ERR) is considered a promising strategy for low-temperature NH_3 synthesis. Moreover, the conversion of NO_3^- into usable NH_3 also solves the NO_3^- pollution problem.

NO_3^- electroreduction to ammonia (NO_3^--to-NH_3) is a multi-electron reduction process ($NO_3^- + 9H^+ + 8e^- \rightarrow NH_3 + 3H_2O$) involving the transfer of 9 protons and 8 electrons.[9–11] Concurrently, various undesired by-products (i.e., NO_2, N_2 and N_2H_4) are usually unavoidable. Therefore, the selectivity and Faradic efficiency of NO_3^--to-NH_3 are relatively low. To achieve efficient conversion of NO_3^--to-NH_3, various metal catalysts, such as Pt,[12–14] Ru,[15] Rh,[16] Ir,[17] Pd,[18] Ag,[19] Sn,[20] Cu,[21] Co,[22] etc., have been investigated for NO_3^--ERR. The reaction pathway at metal electrodes generally involves first the conversion of nitrate to nitrite ($NO_3^- \rightarrow NO_2^-$) and then the formation of strongly adsorbed NO.[23] However, the initial adsorption of NO_3^- species is weak, which is strongly restrained by some co-adsorbates (e.g., HSO_4^- ion and H atom). Therefore, the electroreduction of NO_3^- in H_2SO_4 solution is a great challenge for metal electrodes with strong adsorptivity for HSO_4^- and H species.

Among these metal materials, Pt-based materials are able to achieve electrochemical NO_3^- reduction at a smaller overpotential in the absence of other interfering adsorbates.[13] To further improve catalytic activity and selectivity morphology control and component modulation can be used to design Pt-based catalysts. For example, metallene with two-dimension-

[1] *Key Laboratory of Macromolecular Science of Shaanxi Province, School of Materials Science and Engineering, Shaanxi Normal University, Xi'an 710062, China*

[2] *School of Chemistry and Chemical Engineering, Huazhong University of Science and Technology, Wuhan 430074, China*

* Corresponding author, E-mail: lifuminxs@gmail.com; ndchenyu@gmail.com

Received 27 December 2022; Accepted 2 February 2023; Published online

DOI: 10.54227/elab.20220022

al (2D) characteristics has an ultrathin structure at the atomic level, which shows great potential as a candidate for highly efficient catalyst due to structural advantages such as short carrier diffusion paths, high specific surface area, ample vacancy-type defects, and abundant exposed edge atoms.[24–27] In terms of composition, various bimetallic electrocatalysts have demonstrate better NO_3^--ERR activity compared to monometallic catalysts.[28,29] Bimetallic effects (i.e., electronic and ligand effects) can effectively regulate the adsorption energy of intermediates on active sites during NO_3^--ERR and largely affect the NO_3^- conversion efficiency and product selectivity. In addition, as a unique bimetallic material, intermetallic compounds with ordered crystal structures often exhibit superior activity and durability compared to disordered substituted alloys.[30–34] From the above analysis, the design and development of Pt-based metallene with ordered atomic structure is expected to promote the directional conversion of NO_3^--to-NH_3.

For the actual NO_3^- reduction technology, the cathodic NO_3^--ERR and the anodic oxygen evolution reaction (OER) form a loop in the electrolysis process. Unfortunately, the sluggish and complex OER kinetics usually requires an anode potential greater than 1.5 V to drive, which limits the overall electrolysis efficiency. Therefore, in view of practicability and cost, it may be possible to replace OER with other electrooxidation reactions with low oxidation potential. For example, the anodic electrooxidation of organic small molecules as an alternative to OER electrolysis for hydrogen production has been extensively studied.[35–38] However, the introduction of favorable small molecule oxidation reactions to enhance the electrochemical production of NH_3 has not been discussed in depth. Formic acid (HCOOH) is considered as an excellent energy carrier due to its low toxicity, accessibility and non-flammability.[39–42] The formic acid oxidation reaction (FAOR) only requires two electrons and two protons for complete oxidation to CO_2 and has onset an oxidation potential about 0.1-0.2 V.[43] Therefore, replacing the anodic OER with FAOR may be an effective and valuable strategy to reduce the total electrolytic voltage for NH_3 electroproduction.

In this work, intermetallic PtTe metallene (PtTe-ML) with ultrathin thickness is easily synthesized by a simple liquid-phase chemical reduction method, which shows excellent electroactivity for both NO_3^--ERR and FAOR. Due to the 2D ultrathin morphology and the interaction between Pt and Te atoms, PtTe-ML exhibits significantly enhanced electrocatalytic performance, in which the NH_3 production rate for the electrocatalytic conversion of NO_3^--to-NH_3 is 2.32 mg h^{-1} mg_{cat}^{-1} at −0.04 V potential with a Faradic efficiency of 95.5%. Besides, PtTe-ML optimizes the reaction pathway of FAOR, which achieves a significant negative shift in the onset oxidation potential of FAOR (0.125 V). Thus, bifunctional PtTe-ML can realize energy-saving electrochemical NH_3 production during the FAOR assisted NO_3^--ERR.

Experimental section

Reagents and chemicals

Platinum acetylacetonate ($Pt(acac)_2$), telluric acid (H_6TeO_6, 98%), and formic acid (HCOOH) were obtained from Aladdin Industrial Co., Ltd. N,N-dimethylacetamide (C_4H_9NO), polyvinylpyrrolidone (PVP, average molecular weight 5000), acetone (C_3H_6O), and ethanol (C_2H_5OH) were acquired from Sinopharm Chemical Reagent Co., Ltd. Commercial Pt black was achieved from Johnson Matthey Corporation (Figure S1).

Synthesis of PtTe-ML

30 mg of $Pt(acac)_2$ and 13 mg of H_6TeO_6 were added in 30 mL of N,N- dimethylacetamide, and then 600 mg of PVP and 0.06 mL of formic acid were added. After 30 min, the mixture was poured into a Teflon pressure reactor. After injecting CO to 0.5 bar, the mixture was heated to 160 °C and kept for 2 hours under magnetic stirring. Finally, the product was washed 3 times with a mixture of acetone and ethanol and freeze-dried.

Physical characterization, electrochemical test, theoretical calculation, and detection of products

The experimental details about physical characterization, electrochemical test, theoretical calculation, and detection of products were provided in Supplemental Information.

Results and discussion

Characterization of PtTe-ML

PtTe-ML was synthesized by liquid-phase chemical reduction method with $Pt(acac)_2$, H_6TeO_6, HCOOH, PVP and N,N-dimethylacetamide as raw materials (Scheme 1). The powder X-ray diffraction (XRD) data of the product matches well with the standard XRD data (PtTe JCPDS no. 22-0783), indicating the successful synthesis of PtTe intermetallic compound (Figure 1a). Energy dispersive X-ray spectroscopy (EDX) data further confirms that the product contains Pt and Te elements with an atomic ratio of Pt/Te of 50.07:49.93, close to the theoretical atomic ratio (1:1) of PtTe intermetallic compound (Figure 1b).

X-ray photoelectron spectroscopy (XPS) characterization were performed to analyze the valence and electronic properties of Pt and Te atoms in PtTe-ML. The XPS survey spectrum confirms that PtTe-ML consists of Pt and Te elements (Figure S2). Pt 4*f* and Te 3*d* spectra were fitted as double peaks including both metals and metal oxides. The peaks at 71.55 eV and 74.88 eV correspond to Pt^0 $4f_{7/2}$ and Pt^0 $4f_{5/2}$, respectively. The Pt^0 $4f_{7/2}$ binding energy of PtTe-ML is located at 71.55 eV (Figure 1c), which is positively shifted by 0.35 eV compared to the standard value (71.20 eV) of Pt metal, indicating the Pt in PtTe-ML is electron-deficient. The binding energy of Te in PtTe- ML ($3d_{5/2}$=572.90 eV) is negatively shifted by 0.20 eV compared to the standard binding energy of Te ($3d_{5/2}$=573.10 eV) (Figure 1d), revealing the transfer of electrons from Pt to Te. In fact, according to the electronegativity (χ), the electrons tend to flow from Te (χ_{Te}=2.1) to Pt (χ_{Pt}=2.2). This anomalous XPS result may originate from the strong interaction

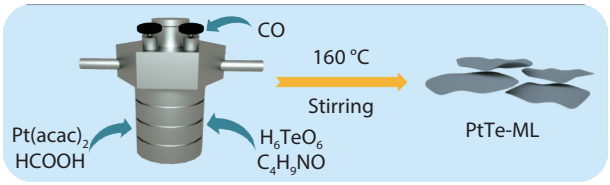

Scheme 1 Schematic illustration for PtTe-ML synthesis.

DOI: 10.54227/elab.20220022

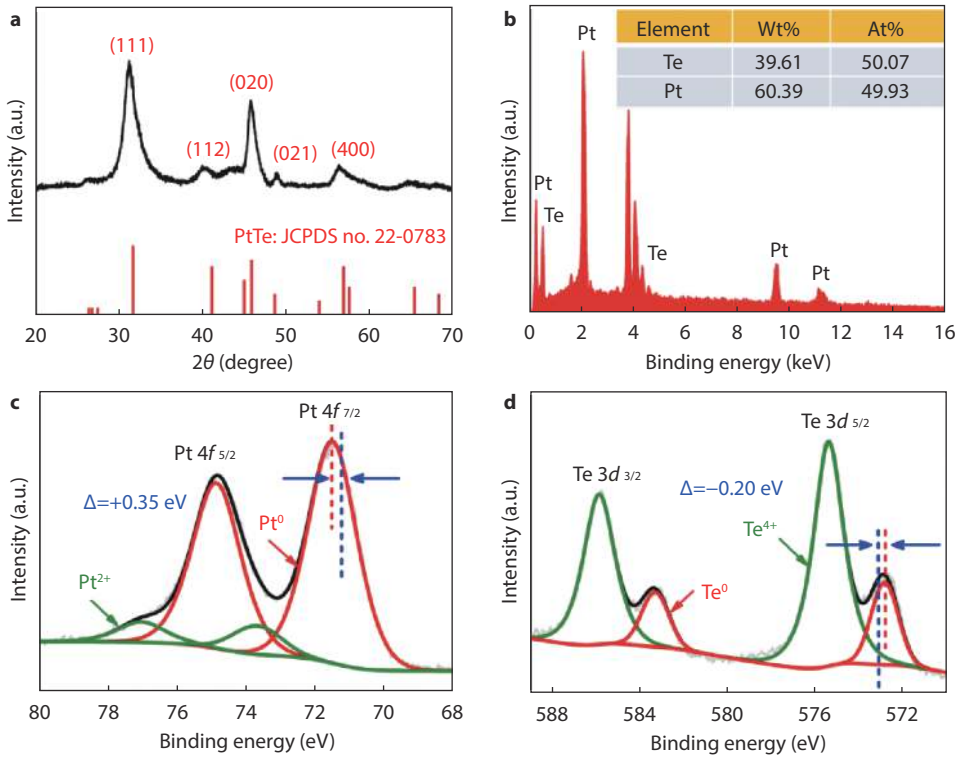

Fig. 1 **a** XRD pattern and **b** EDX spectrum of PtTe-ML. **c** Pt 4*f* and **d** Te 3*d* XPS spectra of PtTe-ML. The blue dotted lines in 1c and 1d represent the standard binding energy values of Pt and Te, respectively.

between Pt and Te in the PtTe intermetallic compound.[33,44,45]

Transmission electron microscopy (TEM) image shows that PtTe-ML has a typical 2D sheet structure (Figure 2a). The control experiments show that PVP plays an important role in the morphology control of PtTe, which ensures the formation of ultra-thin 2D structure (Figures S3). According to the size histogram, the average broadening of individual nanosheets size is about 90 nm. The lattice spacing measured on the magnified HRTEM image is 0.283 nm and 0.198 nm (Figure 2b), corresponding to the PtTe(111) and PtTe(020) crystal planes, respectively. The dark region in the magnified HRTEM pattern corresponds to the nanosheet perpendicular to substrate, which can be applied to preliminarily evaluate the thickness of 2D nanosheet. The width of the linear region is about 2.0 nm (Figure 2b), indicating the thickness of PtTe-ML. The selected area electron diffraction (SAED) pattern of PtTe-ML is coincident with the crystallographic properties of PtTe intermetallic compound (Figure 2c). High-angle annular dark-field scanning TEM (STEM) image (Figure 2d) reveals the presence of folds between PtTe-ML nanosheet layers, which effectively suppresses inter-sheet stacking and facilitates mass transfer. In contrast to the weak luminescence of the substrate, the thin nature of the nanosheets is implied. Furthermore, atomic force microscopy (AFM) image and associated height data confirm that the thickness of 2D nanosheets is only about 2.0 nm (Figure 2e). EDX patterns and line scan results show that Pt and Te are uniformly distributed in the sample (Figure 2f). The above results fully demonstrate the successful synthesis of the PtTe-ML intermetallic compound.

The cathodic NO_3^--ERR at PtTe-ML

Electrochemical measurements were carried out in an H-type electrolyzer using a conventional three-electrode system to study NO_3^--ERR activity of PtTe-ML at 30 °C . All potentials mentioned in the work correspond to the reversible hydrogen electrode potential (RHE). Herein, linear sweep voltammetry (LSV) tests were carried out in 0.5 M H_2SO_4 + 50 mM KNO_3 electrolyte and 0.5 M H_2SO_4 electrolyte, respectively. The obtained LSV curve in 0.5 M H_2SO_4 + 50 mM KNO_3 shows a greater cathodic current with respect to that in 0.5 M H_2SO_4, confirming that PtTe-ML have an electrocatalytic activity for NO_3^--ERR (Figure 3a). In contrast, commercial Pt black exhibits a lower reduction current after adding KNO_3 to electrolyte, suggesting a poor NO_3^--ERR activity (Figure S4). In fact, NO_3^--ERR and HER will compete for active sites, so HER activities of PtTe-ML and commercial Pt black will directly affect their NO_3^--ERR activities. As expected, the HER activity of PtTe-ML is much lower than that of commercial Pt black, which means that PtTe-ML have more active sites for NO_3^--ERR under the same potential, resulting in boosted NO_3^--ERR activity. For commercial Pt black with a high HER activity, the initial adsorption of NO_3^- on Pt atoms is severely inhibited by co-adsorbates H (Figure S4). These electrochemical data reveal that the introduction of Te weakens the intrinsic HER activity of Pt in PtTe-ML (Figure S5), which enhances its NO_3^--ERR activity.

The selectivity of PtTe-ML in the NO_3^--to-NH_3 process was further evaluated at different applied potentials (Figure S6a). After the chronoamperometry test, NH_3 in the electrolyte was detected by ultraviolet-visible (UV-vis) spectroscopy (Figure S6b) and the Faradic efficiency and NH_3 yield were calculated from the corresponding calibration curves (Figure S7). In the range from –0.01 to –0.1 V potential, both the Faradaic effi-

DOI: 10.54227/elab.20220022

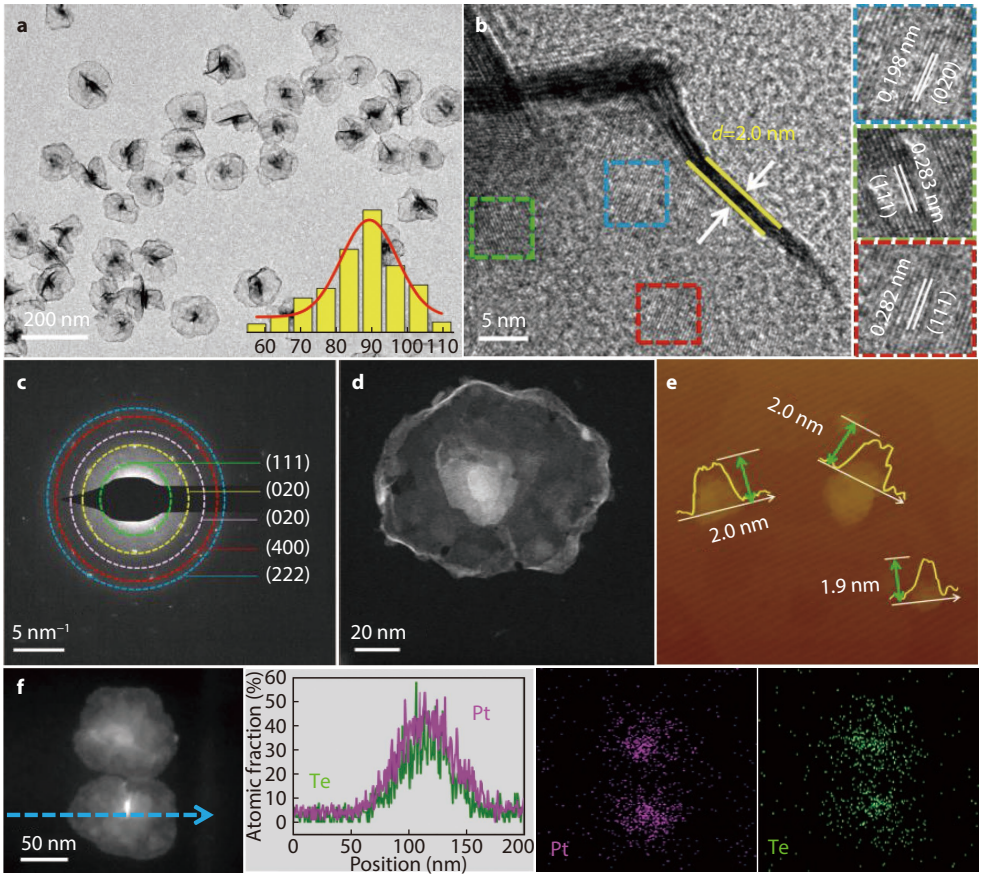

Fig. 2 **a** TEM image and size distribution histogram, **b** HRTEM image and magnified HRTEM image, **c** SAED pattern, **d** STEM image, and **e** AFM image of PtTe-ML. **f** STEM image and corresponding EDX mapping and line scanning of PtTe-ML.

ciency of NO_3^--ERR and NH_3 yield show volcano-like variation, reaching a maximum at −0.04 V (Figure 3b). Specifically, the NH_3 yield and the Faradaic efficiency of NO_3^--ERR on PtTe-ML are 2.32 mg h^{-1} mg_{cat}^{-1} and 95.5% at −0.04 V, respectively, which are much bigger than that of commercial Pt black (0.28 mg h^{-1} mg_{cat}^{-1} and 6.8%) (Figure 3c). In addition, PtTe-ML also shows higher Faradaic efficiency and NH_3 yield of NO_3^--to-NH_3 than most reported electrocatalysts (Table 1), further confirming the high NO_3^--ERR activity of PtTe-ML. To investigate the durability of PtTe-ML for NO_3^--ERR, six consecutive electrolysis cycles were performed. At −0.04 V, the NH_3 yield and the Faradaic efficiency did not fluctuate significantly over the six reaction cycles, implying the PtTe-ML processes good durability for NO_3^--ERR (Figure 3d). During 20 h of NO_3^--ERR electrolysis, the current density exhibits little variation (Figure S8). After long time electrolysis, TEM (Figure S9a), EDX (Figure S9b) and XPS (Figures S9c and S9d) characterizations reveal that the morphology, component, and valence state of PtTe-ML are almost unchanged, suggesting the good stability of PtTe-ML for NO_3^--ERR.

To clarify the origin of NO_3^--ERR activity, density functional theory (DFT) calculations were carried out to understand the reaction mechanism of NO_3^--ERR on PtTe-ML. The Pt(111) and PtTe(111) surfaces were constructed to gain insight into the Pt electronic structure and the adsorption behaviours of H*, NO_3* and intermediates (Figure 4a). The projected density of states (PDOS) analysis disclosed that Te atoms on the PtTe(111) surface regulate the 5d orbitals of Pt, showing a left shifted PDOS and a downshifted d band center (ε_d=−3.15 eV) of Pt with respect to that of the Pt(111) surface (ε_d=−2.31 eV) (Figure 4b). Generally, the negative ε_d value indicates the rather weak interaction between Pt atoms and adsorbates (i.e., NO_3* and intermediates), which may further optimize the NO_3^--ERR process on the PtTe(111) surface. Subsequently, free energy diagrams of NO_3^--ERR on the Pt(111) and PtTe(111) surfaces are further investigated to validate the NO_3^--to-NH_3 performance of PtTe-ML (Figure 4c). Firstly, NO_3^- will spontaneously adsorb on the surfaces of the two catalysts with a decrease in total energy. Then, the adsorbed NO_3* is reduced by splitting the N-O bond to form NO_2*, NO* and HNO* with a continuous decrease in total energy. Thereafter, the formation of NH* from HNO* on the Pt(111) surface (4.53 eV) is an endothermic process with a high energy barrier. This result indicates that HNO* intermediates, like toxic species, can poison Pt active sites on the Pt(111) surface, which is consistent with the low activity of Pt black for NO_3^--ERR. In contrast, the reduction of HNO* and all subsequent hydrogenation steps are exothermic on the PtTe(111) surface. Therefore, PtTe-ML can improve both NO_3^--ERR activity and selectivity with respect to Pt black. All experiments and theoretical simulations reveal that Te atoms can modulate εd of Pt atoms in PtTe-ML, thus optimizing the binding of the intermediates on Pt atoms, avoiding the poisoning of Pt active sites and in turn achieving an enhanced NO_3^--to- NH_3 process.

DOI: 10.54227/elab.20220022

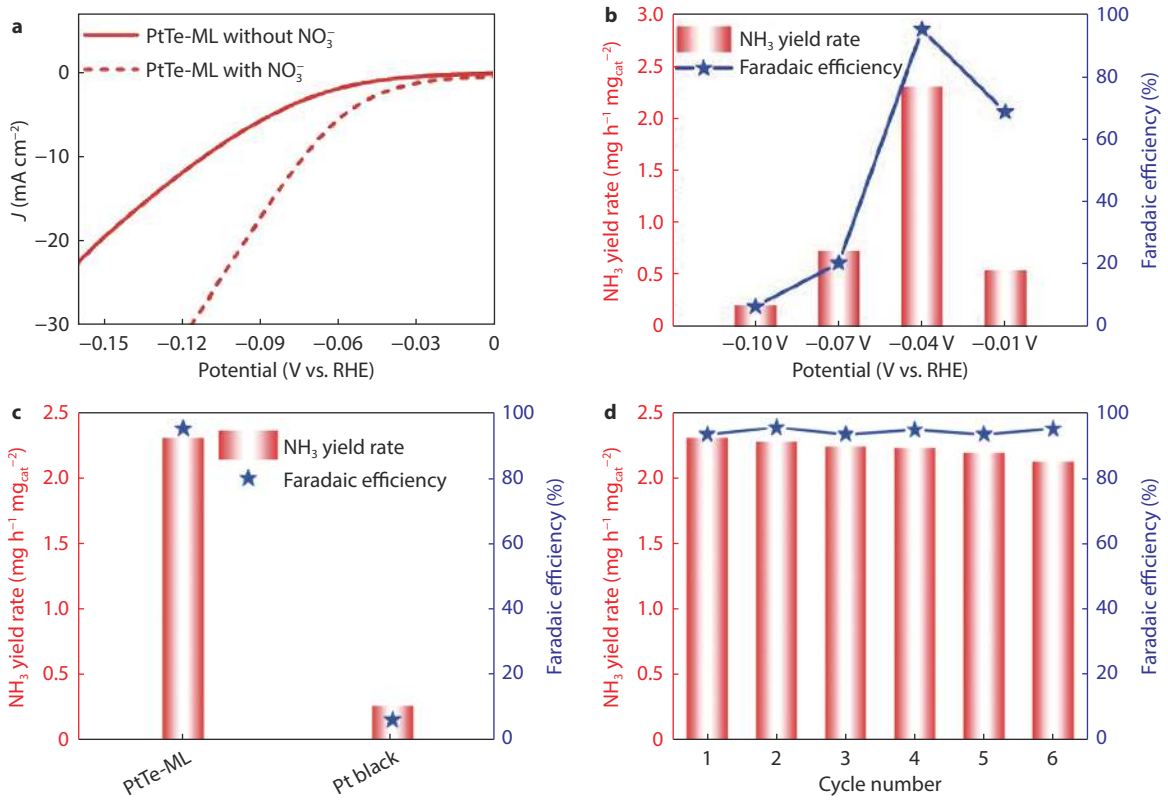

Fig. 3 **a** LSV curves of PtTe-ML in Ar-saturated 0.5 M H_2SO_4 electrolyte with and without 50 mM KNO_3 at 50 mV s^{-1}. **b** The Faradaic efficiency of NO_3^--ERR and NH_3 yield of PtTe-ML at different potentials. **c** NH_3 yields and Faradaic efficiency of PtTe-ML and commercial Pt black at −0.04 V potential. **d** The as-obtained Faradaic efficiency and NH_3 yield during cyclic stability test of PtTe-ML.

Table 1. Faradic efficiency and NH_3 yield of NO_3^--ERR at various electrocatalysts.

Catalysts	Electrolyte	Applied potential (vs. RHE)	Performance	Ref. (year)
PtTe-ML	0.5 M H_2SO_4+50 mM KNO_3	−0.04 V	r_{NH3}: 2.32 mg h^{-1} mg$_{cat}^{-1}$ FE_{NH3}: 95.5%	This Work
Polyaniline-modified CuO nanowire	0.5 M K_2SO_4+14.3 mM KNO_3	−0.64 V	r_{NH3}: 0.213 mmol h^{-1} cm^{-2} FE_{NH3}: 91.38%	2023[52]
Polycrystalline Cu	0.5 M K_2SO_4+0.1 M KNO_3	−0.266 V	r_{NH3}: 0.1014 mmol h^{-1} cm^{-2} FE_{NH3}: 93.91%	2022[53]
RhCu Bimetallic Nanocubes	0.1 M $HClO_4$+0.05 M KNO_3	0.05 V	r_{NH3}: 2.40 mg h^{-1} mg$_{cat}^{-1}$ FE_{NH3}: 93.7%	2022[16]
FeOOH nanorods	0.1 M PBS+0.1 M $NaNO_3$	−0.50 V	r_{NH3}: 2.419 mg h^{-1} cm^{-2} FE_{NH3}: 92%	2022[54]
Pd–PdO-modified Co_3O_4 nanowires	0.5 M K_2SO_4+14.3 mM KNO_3	−0.64 V	r_{NH3}: 0.2044 mmol h^{-1}cm^{-2} FE_{NH3}: 88.6%	2022[55]
CuPd aerogels	0.5 M K_2SO_4+3.57 mM KNO_3	−0.46 V	r_{NH3}: 0.784 mg h^{-1} mg$_{cat}^{-1}$ FE_{NH3}: 90.02%	2021[29]
Cu nanoplates	0.5 M K_2SO_4+3.57 mM KNO_3	−0.65 V	r_{NH3}: 0.781 mg h^{-1} mg$_{cat}^{-1}$ FE_{NH3}: 93.26%	2021[56]
Pd concave nanocubes	0.1 M NaOH+20 mM $NaNO_3$	−0.2 V	r_{NH3}: 0.307 mg h^{-1} mg^{-1} Pd FE_{NH3}: 35.1%	2021[57]

Anodic FAOR at PtTe-ML

To couple anodic FAOR with cathodic NO_3^--ERR, the FAOR activity of PtTe-ML was studied. Cyclic voltammetry (CV) was used to test the electrochemical behaviours of PtTe-ML and commercial Pt black in 0.5 M H_2SO_4 solution. Compared with commercial Pt black, the hydrogen absorption/desorption area of PtTe-ML is completely suppressed due to the introduction of Te that modifies the Pt electronic structure and affects the adsorption/desorption behaviour of H atoms on the PtTe-ML surface (Figure 5a).[46,47] Concurrently, PtTe-ML is inert to methanol oxidation reaction, which means that PtTe-ML cannot provide three consecutive Pt atoms for methanol adsorption and electrooxidation (Figure 5b). This result is attributed to the fact that Pt atoms on the PtTe-ML surface is effectively isolated by Te atoms, and this special Pt coordination environment of PtTe-ML is desired by FAOR.

The FAOR on Pt surface generally follows a two-pathway mechanism. The direct dehydrogenation pathway refers to the direct electrooxidation of formic acid into CO_2 at a low anodic potential, and the indirect pathway involves the generation of adsorbed CO_{ad}, which needs to be further electrooxidized to CO_2 at a higher potential.[34,48] In fact, CO_{ad} is easily adsorbed on the Pt surface, leading to catalyst deactivation. Thus, the key to elevate the FAOR activity of Pt-based electrocatalysts is to strengthen the direct dehydrogenation pathway, in which the separation of continuous Pt active sites is a proven efficient strategy.[47,49–51] As revealed by the forward scan curves of FAOR, PtTe-ML shows a clear oxidation peak

DOI: 10.54227/elab.20220022

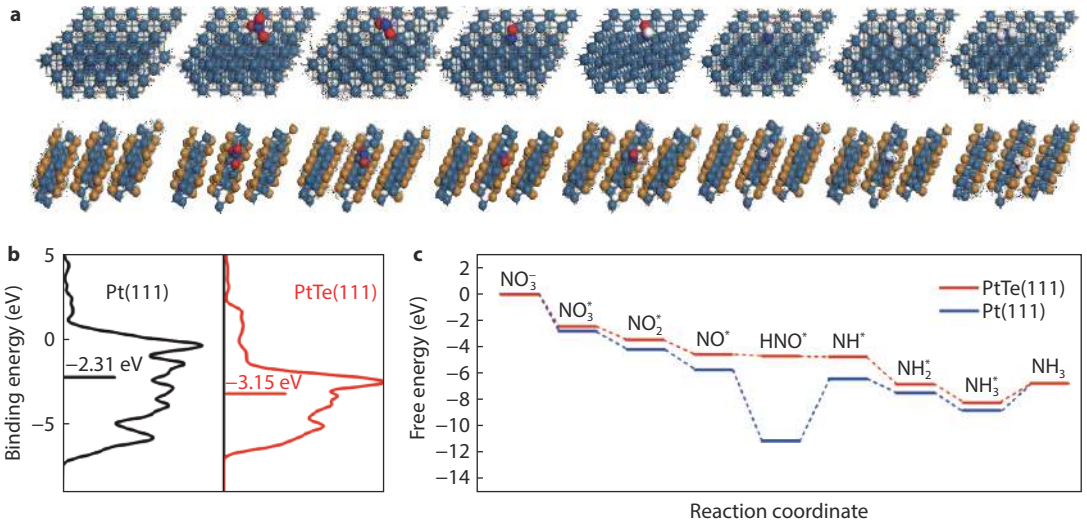

Fig. 4 **a** Atomic structure of the Pt(111) and PtTe(111) surface adsorbed with NO_3* and intermediates. **b** Calculated d-band center values of PtTe(111) and Pt(111) surfaces. **c** The free energy diagrams of NO_3^--ERR on the Pt(111) and PtTe(111) surfaces.

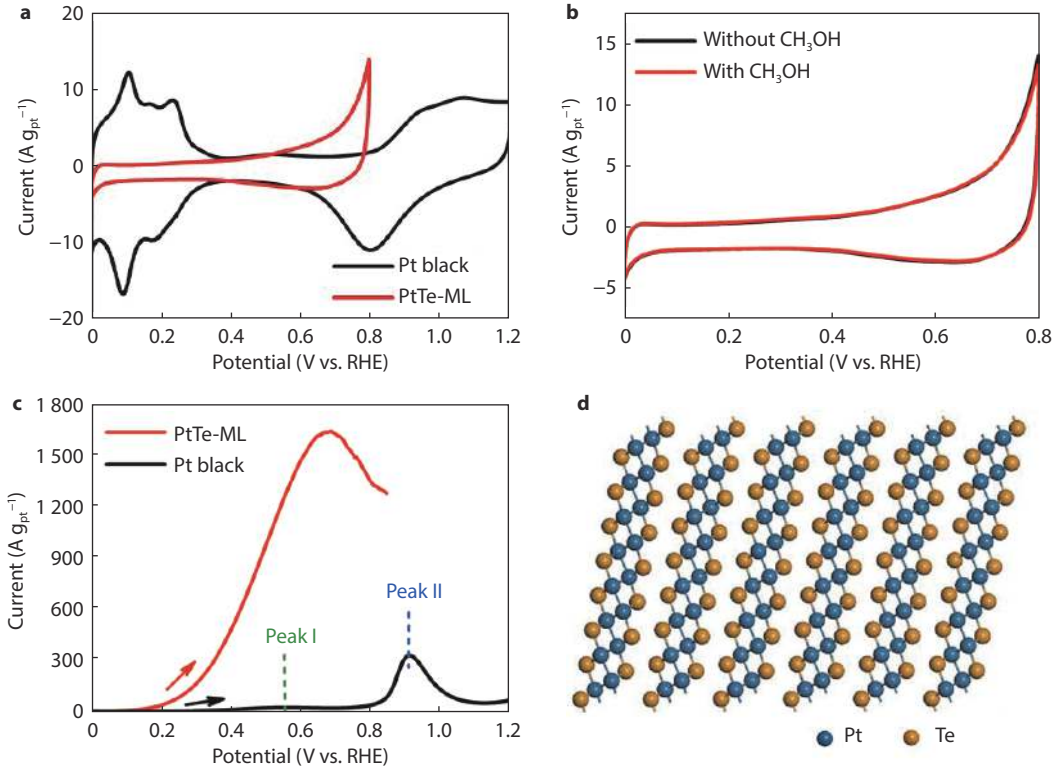

Fig. 5 **a** CV curves of PtTe-ML and commercial Pt balck in Ar-saturated 0.5 M H_2SO_4 electrolyte at 50 mV s^{-1}. **b** CV curves of PtTe-ML in Ar-saturated 0.5 M H_2SO_4 electrolyte in the presence or absence of 0.5 M CH_3OH at 50 mV s^{-1}. **c** LSV curves of PtTe-ML and Pt balck in 0.5 M H_2SO_4 and 0.5 M HCOOH electrolyte at 50 mV s^{-1}. **d** Atomic structure of PtTe-ML.

appears at 0.672 V, indicating a direct dehydrogenation oxidation pathway (Figure 5c). For PtTe-ML, the adjacent Pt atoms are interrupted by Te atoms, producing abundant single or double Pt atoms and in turn making the dehydrogenation pathway dominant at PtTe-ML. The ball-and-stick model of PtTe-ML clearly show that the Te atoms successfully isolate the consecutive Pt atoms (Figure 5d). In the high potential range, the Te atoms on the PtTe-ML surface inevitably undergo the dissolution and the rearrangement of Pt atoms also occurs simultaneously. The CV curves of PtTe-ML in the high potential range (0-1.2 V) show a distinctive oxidation peak of Te (Figure S10a). The oxidation peak current gradually decreases with scanning cycles. Meanwhile, the exposure of hydrogen absorption/desorption area also occurs, which originates from the electrochemical oxidation of Te and further exposure to the internal Pt atoms. The changes in FAOR pathway at

DOI: 10.54227/elab.20220022

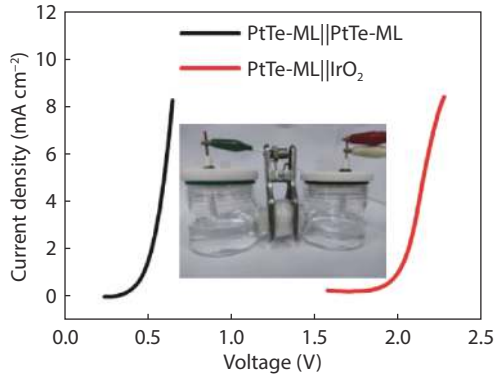

Fig. 6 Polarization curves of PtTe-ML||PtTe-ML electrolyzer in 0.5 M H_2SO_4 + 50 mM KNO_3 + 0.5 M HCOOH solution and PtTe-ML||IrO_2 electrolyzer in 0.5 M H_2SO_4.

PtTe-ML were studied by continuous CV tests (Figure S10b). The continuous dissolution of Te atoms in PtTe-ML makes Pt atoms contact with each other, leading to a change in the oxidation pathway and a sharp current decay. To avoid the dissolution of Te, the potential range of FAOR performance tests was limited to 0-0.8 V for PtTe-ML. In contrast, Pt black displays a main oxidation at around 0.94 V that corresponds to the oxidation of CO_{ad} formed via an indirect pathway of FAOR. Benefiting from the optimized FAOR pathway, the Pt-mass activity of PtTe-ML (1640 A g_{Pt}^{-1}) for the FAOR is 55 times bigger than that of commercial Pt black (30 A g_{Pt}^{-1}) at 0.672 V potential (Figure 5c).

The stability of the electrocatalysts is highly important for their practical application. The electrochemical stability was evaluated by recording current-time curves at 0.6 V potential. After a course of 10,000 s, the FAOR current at PtTe-ML is much higher than that at commercial Pt black, indicating the good durability of PtTe-ML (Figure S11). After stability test, EDX, XPS and TEM characterizations show that PtTe-ML retains its initial crystal structure, component and morphology, confirming its good long-term stability (Figure S12).

FAOR assisted NO_3^--ERR at bifunctional PtTe-ML

The above electrochemical measurements show that PtTe-ML has good catalytic performance for both FAOR and NO_3^--ERR. Thus, a two-electrode cell for the FAOR assisted NO_3^--ERR was constructed by using PtTe-ML as both anode and cathode (i.e., PtTe-ML||PtTe-ML electrolyzer), respectively. In the presence of HCOOH, the PtTe- ML||PtTe-ML electrolyzer requires only a total voltage of 0.4 V to drive. An OER- coupled NO_3^--ERR double electrolyzer (i.e., PtTe-ML||IrO_2 electrolyzer) was also constructed with IrO_2 as the anode and PtTe-ML as the cathode, respectively. In the absence of HCOOH, the PtTe-ML||IrO_2 electrolyzer requires up to 2.0 V to drive. This result suggests that FAOR-assisted NO_3^--ERR can provide higher energy conversion efficiency for NH_3 electroproduction compared to conventional OER-coupled NO_3^--ERR.

Conclusions

In summary, we effectively promote an energy-saving NH_3 electroproduction by coupling anodic FAOR with cathodic NO_3^--ERR using PtTe-ML as bifunctional electrocatalyst. The intermetallic PtTe metallene has the ultrathin 2D nanosheet structure, which provides abundant active sites for NO_3^--ERR and FAOR. With the introduction of Te, the HER activity of Pt is weakened and the catalytic activity of NO_3^--ERR is increased on PtTe-ML. DFT calculations show that Te atoms can modulate the εd of Pt atoms in PtTe-ML, thus optimizing the binding of intermediates on Pt atoms and thus achieving an enhanced NO_3^--to-NH_3 process. Under the applied potential of –0.04 V, the ammonia faradaic efficiency and ammonia production rate over the PtTe-ML can reach 95.5% and 2.32 mg h^{-1} mg_{cat}^{-1}, respectively, which are far higher than Pt black. At the same time, Te atoms separate the continuous Pt atoms, and optimize the FAOR pathway on PtTe-ML, resulting in enhanced FAOR activity. The successful construction of FAOR assisted NO_3^--ERR electrolyzer confirms the feasibility of promoting energy-saving NO_3^--to-NH_3 by optimizing anodic reaction and developing efficient bifunctional electrocatalysts.

■ ACKNOWLEDGEMENTS

This research was sponsored by the National Natural Science Foundation of China (22272103 and 22202076), the China Postdoctoral Science Foundation (2022M711231), Science and Technology Innovation Team of Shaanxi Province (2023-CX-TD-27), the Young Scientist Innovation Project of School of Materials Science and Engineering at Shaanxi Normal University (2022YSIP-MSE-SNNU005), and Fundamental Research Funds for the Central Universities (GK202202001).

■ SUPPLEMENTAL INFORMATION

Additional results for experimental details for the physical characterization, electrochemical test, theoretical calculation, and detection of products.

■ CONFLICT OF INTEREST

The authors declare no conflict of interest.

■ AUTHOR CONTRIBUTIONS

Yu Chen and Fu-Min Li supervised the project. Qing-Ling Hong designed the experiments and wrote the manuscript. Bo-Qiang Miao, and Tian-Jiao Wang discussed the experiment results. All authors have given approval to the final version of the paper.

■ REFERENCES

1. T. Ren, K. Ren, M. Wang, M. Liu, Z. Wang, H. Wang, X. Li, L. Wang and Y. Xu, *Chem. Eng. J.*, 2021, 426, 130759
2. J. Yu, B. Chang, W. Yu, X. Li, D. Wang, Z. Xu, X. Zhang, H. Liu and W. Zhou, *Carbon Energy*, 2022, 4, 237
3. P. H. van Langevelde, I. Katsounaros and M. T. M. Koper, *Joule*, 2021, 5, 290
4. J. Yao and J. Yan, *Sci. China. Chem.*, 2020, 63, 1737
5. S. Mukherjee, D. A. Cullen, S. Karakalos, K. Liu, H. Zhang, S. Zhao, H. Xu, K. L. More, G. Wang and G. Wu, *Nano Energy*, 2018, 48, 217
6. Q. Yao, J. Chen, S. Xiao, Y. Zhang and X. Zhou, *ACS Appl. Mater. Interfaces*, 2021, 13, 30458
7. Y. Sun, W. Wu, L. Yu, S. Xu, Y. Zhang, L. Yu, B. Xia, S. Ding, M. Li, L. Jiang, J. Duan, J. Zhu and S. Chen, *Carbon Energy*, 2022, 1, 1
8. Y. Zeng, C. Priest, G. Wang and G. Wu, *Small Methods*, 2020, 4,

DOI: 10.54227/elab.20220022

2000672
9. S. Garcia-Segura, M. Lanzarini-Lopes, K. Hristovski and P. Westerhoff, *Appl. Catal. B Environ.*, 2018, 236, 546
10. Y. Yao, S. Zhu, H. Wang, H. Li and M. Shao, *Angew. Chem. Int. Ed.*, 2020, 59, 10479
11. X. Yang, S. Sun, L. Meng, K. Li, S. Mukherjee, X. Chen, J. Lv, S. Liang, H.-Y. Zang, L.-K. Yan and G. Wu, *Appl. Catal. B Environ.*, 2021, 285, 119794
12. G. A. Attard, J. Souza-Garcia, R. Martinez-Hincapie and J. M. Feliu, *J. Catal.*, 2019, 378, 238
13. M. Duca, N. Sacre, A. Wang, S. Garbarino and D. Guay, *Appl. Catal. B Environ.*, 2018, 221, 86
14. Z. Mumtarin, M. M. Rahman, H. M. Marwani and M. A. Hasnat, *Electrochim. Acta*, 2020, 346, 135994
15. R. Chauhan and V. C. Srivastava, *Chem. Eng. J.*, 2020, 386, 122065
16. Z. X. Ge, T. J. Wang, Y. Ding, S. B. Yin, F. M. Li, P. Chen and Y. Chen, *Adv. Energy Mater.*, 2022, 12, 2103916
17. J.-Y. Zhu, Q. Xue, Y.-Y. Xue, Y. Ding, F.-M. Li, P. Jin, P. Chen and Y. Chen, *ACS Appl. Mater. Interfaces*, 2020, 12, 14064
18. J. Li, G. Zhan, J. Yang, F. Quan, C. Mao, Y. Liu, B. Wang, F. Lei, L. Li, A. W. M. Chan, L. Xu, Y. Shi, Y. Du, W. Hao, P. K. Wong, J. Wang, S.-X. Dou, L. Zhang and J. C. Yu, *J. Am. Chem. Soc.*, 2020, 142, 7036
19. J. Liu, T. Cheng, L. Jiang, A. Kong and Y. Shan, *ACS Appl. Mater. Interfaces*, 2020, 12, 33186
20. S. Luo, W. Chen, Y. Cheng, X. Song, Q. Wu, L. Li, X. Wu, T. Wu, M. Li, Q. Yang, K. Deng and Z. Quan, *Adv. Mater.*, 2019, 31, 1903683
21. T. Zhu, Q. Chen, P. Liao, W. Duan, S. Liang, Z. Yan and C. Feng, *Small*, 2020, 16, 2004526
22. J. Gao, B. Jiang, C. Ni, Y. Qi, Y. Zhang, N. Oturan and M. A. Oturan, *Appl. Catal. B Environ.*, 2019, 254, 391
23. I. Katsounaros and G. Kyriacou, *Electrochim. Acta*, 2008, 53, 5477
24. M. Bat-Erdene, A. S. R. Bati, J. Qin, H. Zhao, Y. L. Zhong, J. G. Shapter and M. Batmunkh, *Adv. Funct. Mater.*, 2022, 32, 2107280
25. H. Yang, F. He, J. Shen, Z. Chen, Y. Yao, L. He and Y. Yu, *Energy Lab*, 2022, 1, 220007
26. L. Zeng, W. Chen, Q. Zhang, S. Xu, W. Zhang, F. Lv, Q. Huang, S. Wang, K. Yin, M. Li, Y. Yang, L. Gu and S. Guo, *ACS Catal.*, 2022, 12, 11391
27. H. Yu, T. Zhou, Z. Wang, Y. Xu, X. Li, L. Wang and H. Wang, *Angew. Chem. Int. Ed. Engl.*, 2021, 60, 12027
28. P. Mirzaei, S. Bastide, A. Aghajani, J. Bourgon, E. Leroy, J. Zhang, Y. Snoussi, A. Bensghaier, O. Hamouma, M. M. Chehimi and C. Cachet-Vivier, *Langmuir*, 2019, 35, 14428
29. Y. Xu, K. Ren, T. Ren, M. Wang, M. Liu, Z. Wang, X. Li, L. Wang and H. Wang, *Chem. Commun.*, 2021, 57, 7525
30. M. Armbrüster, K. Kovnir, M. Behrens, D. Teschner, Y. Grin and R. Schlögl, *J. Am. Chem. Soc.*, 2010, 132, 14745
31. Y. S. Kang, D. Choi, J. Cho, H.-Y. Park, K.-S. Lee, M. Ahn, I. Jang, T. Park, H. C. Ham and S. J. Yoo, *ACS Appl. Energy Mater.*, 2020, 3, 4226
32. J. Yu, A. F. Kolln, D. Jing, J. Oh, H. Liu, Z. Qi, L. Zhou, W. Li and W. Huang, *ACS Appl. Mater. Interfaces*, 2021, 13, 52073
33. F. Li, Q. Xue, G. Ma, S. Li, M. Hu, H. Yao, X. Wang and Y. Chen, *J. Power Sources*, 2020, 450, 227615
34. L. An, H. Yan, B. Li, J. Ma, H. Wei and D. Xia, *Nano Energy*, 2015, 15, 24
35. S. Liu, S. Yin, L. Cui, H. Yu, K. Deng, Z. Wang, Y. Xu, L. Wang and H. Wang, *Energy Lab*, 2022, 1, 220005
36. T.-J. Wang, H.-Y. Sun, Q. Xue, M.-J. Zhong, F.-M. Li, X. Tian, P. Chen, S.-B. Yin and Y. Chen, *Science Bulletin*, 2021, 66, 2079
37. L. Tao, M. Sun, Y. Zhou, M. Luo, F. Lv, M. Li, Q. Zhang, L. Gu, B. Huang and S. Guo, *J. Am. Chem. Soc.*, 2022, 144, 10582
38. K. Yin, Y. Chao, F. Lv, L. Tao, W. Zhang, S. Lu, M. Li, Q. Zhang, L. Gu, H. Li and S. Guo, *J. Am. Chem. Soc.*, 2021, 143, 10822
39. T.-J. Wang, Y.-C. Jiang, J.-W. He, F.-M. Li, Y. Ding, P. Chen and Y. Chen, *Carbon Energy*, 2022, 4, 283
40. T. Shen, S. Chen, C. Zhang, Y. Hu, E. Ma, Y. Yang, J. Hu and D. Wang, *Adv. Funct. Mater.*, 2022, 32, 2107672
41. W. Liang, Y. Wang, L. Zhao, W. Guo, D. Li, W. Qin, H. Wu, Y. Sun and L. Jiang, *Adv. Mater.*, 2021, 33, 2100713
42. H. Wang, W. Wang, Q. Mao, H. Yu, K. Deng, Y. Xu, X. Li, Z. Wang and L. Wang, *Chem. Eng. J.*, 2022, 450, 137995
43. Q. Xue, X.-Y. Bai, Y. Zhao, Y.-N. Li, T.-J. Wang, H.-Y. Sun, F.-M. Li, P. Chen, P. Jin, S.-B. Yin and Y. Chen, *J. Energy Chem.*, 2022, 65, 94
44. L. Bu, Q. Shao, Y. Pi, J. Yao, M. Luo, J. Lang, S. Hwang, H. Xin, B. Huang, J. Guo, D. Su, S. Guo and X. Huang, *Chem*, 2018, 4, 359
45. K. Kovnir, M. Armbrüs ter, D. Teschner, T. V. Venkov, L. Szentmiklósi, F. C. Jentoft, A. Knop-Gericke, Y. Grin and R. Schlögl, *Surf. Sci.*, 2009, 603, 1784
46. K. Tonnis, Z. Nan, J. Fang, R. Pavlicek, E. S. DeCastro and A. P. Angelopoulos, *ACS Appl. Energy Mater.*, 2020, 3, 7588
47. Z. Peng, H. You and H. Yang, *Adv. Funct. Mater.*, 2010, 20, 3734
48. G.-T. Fu, B.-Y. Xia, R.-G. Ma, Y. Chen, Y.-W. Tang and J.-M. Lee, *Nano Energy*, 2015, 12, 824
49. J. Geng, Z. Zhu, X. Bai, F. Li and J. Chen, *ACS Appl. Energy Mater.*, 2020, 3, 1010
50. S. H. Ahn, Y. Liu and T. P. Moffat, *ACS Catal.*, 2015, 5, 2124
51. A. Ferre-Vilaplana, J. Victor Perales-Rondon, J. M. Feliu and E. Herrero, *ACS Catal.*, 2015, 5, 645
52. Y. Xu, Y. Wen, T. Ren, H. Yu, K. Deng, Z. Wang, X. Li, L. Wang and H. Wang, *Appl. Catal. B Environ.*, 2023, 320, 121981
53. Y. L. Zhao, Y. Liu, Z. J. Zhang, Z. K. Mo, C. Y. Wang and S. Y. Gao, *Nano Energy*, 2022, 97, 107124
54. Q. Liu, Q. Liu, L. Xie, Y. Ji, T. Li, B. Zhang, N. Li, B. Tang, Y. Liu, S. Gao, Y. Luo, L. Yu, Q. Kong and X. Sun, *ACS Appl. Mater. Interfaces*, 2022, 14, 17312
55. M. Liu, Q. Mao, K. Shi, Z. Wang, Y. Xu, X. Li, L. Wang and H. Wang, *ACS Appl. Mater. Interfaces*, 2022, 14, 13169
56. Y. Xu, M. Wang, K. Ren, T. Ren, M. Liu, Z. Wang, X. Li, L. Wang and H. Wang, *J. Mater. Chem. A*, 2021, 9, 16411
57. J. Lim, C.-Y. Liu, J. Park, Y.-H. Liu, T. P. Senftle, S. W. Lee and M. C. Hatzell, *ACS Catal.*, 2021, 11, 7568